Pergamon

Int. J. Heat Mass Transfer. Vol. 40, No. 13, pp. 3163–3176, 1997

Printed in Great Britain
0017-9310/97 $17.00 + 0.00

PII: S0017-9310(96)00367-5

Vortex structure and heat transfer in the stagnation region of an impinging plane jet (simultaneous measurements of velocity and temperature fields by digital particle image velocimetry and laser-induced fluorescence)

JUN SAKAKIBARA, KOICHI HISHIDA† and MASANOBU MAEDA

Department of Mechanical Engineering, Keio University, 3-14-1 Hiyoshi, Kohoku-ku, Yokohama, 223, Japan

(*Received* 26 *March* 1996 *and in final form* 24 *September* 1996)

Abstract—Velocity and temperature in the stagnation region of an impinging plane jet were simultaneously measured by digital particle image velocimetry and laser-induced fluorescence. Counter-rotating vortex pairs observed in the stagnation region sweep cold fluid toward the wall and eject high-temperature fluid toward the outer region. The weighted PDF of the turbulent heat flux indicates that the contribution of this ejection mechanism to the net heat flux is dominant. The streamwise vortex pair is transported from the free-jet region to the stagnation region and the vorticity is amplified by the main stream of what in the vicinity of the wall. © 1997 Elsevier Science Ltd.

1. INTRODUCTION

The high heat transfer rates realized in the stagnation region of turbulent impinging jets have been employed for many practical purposes. Early investigation by Gardon and Akfirat [1] on the heat transfer of impinging jets showed that the average heat transfer rate produced by a single plane jet is dependent on the nozzle-to-plate spacing H, exhibiting a maximum around $H/B = 8$. For high Reynolds numbers the jets are turbulent and the heat transfer rates exceed the laminar solution by nearly a factor of two.

Sutera *et al.* [2, 3] proposed that the augmentation of heat transfer in the stagnation region of Heimenz flow [4] was caused by a strong vortex line embedded in the boundary layer. When the vortex lines oriented normal to the impinging jet and normal to the stagnation line are convected into the stagnation region, the vortex lines are stretched and the vorticity is amplified through conservation of angular momentum. Yokobori *et al.* [5] found counter rotating vortex pairs normal to the stagnation line on a flat surface using a flow visualization. They also visualized the temperature distribution of the hot surface and concluded that a high heat transfer rate was associated with interacting vortical structures. As an alternate case, a blunt body surrounded by homogeneous flow have also similar counter rotating vortex pairs in the stagnation region [6]. The high heat transfer rate was observed at where the velocity between neighboring vortex pairs was directed toward the surface. All of these investigators suggest that the high heat transfer rates are accomplished by coherent vortical structures near the surface transporting the heat from the surface.

By assuming flow symmetry and applying the boundary layer approximation, a mean temperature distribution on a center plane of the impinging jet is a solution of the energy transport equation:

$$V\frac{\partial T}{\partial Y} = \frac{\partial}{\partial Y}\left(a\frac{\partial T}{\partial Y} - \overline{v't'}\right). \tag{1}$$

The solution of equation (1) depends only on the distribution of mean velocity normal to the surface V and the turbulent heat flux $\overline{v't'}$, if the boundary condition and thermal diffusivity a is given. By neglecting a buoyancy force, assuming flow symmetry and applying the boundary layer approximation, V is a solution of the momentum transport equation;

$$V\frac{\partial V}{\partial Y} = -\frac{\partial P}{\partial Y} - \frac{\partial}{\partial Y}\overline{v'v'}. \tag{2}$$

In this equation, a normal component of Reynolds stress $\overline{v'v'}$ might enhance the momentum transport near the surface and it makes higher gradient of V in the vicinity of the surface than that of laminar case. This modification of the V distribution causes modification of T distribution as a solution in equation

† Author to whom correspondence should be addressed

NOMENCLATURE

a thermal diffusivity
B nozzle width
c condition flag
H nozzle-to-plate spacing
I_b fluorescence intensity with no incident light
I_c calibration function of the fluorescence intensity to temperature
I_{ref} fluorescence intensity at fluid temperature of I_b
q_w averaged heat flux from wetted surface of wall
Re_B Reynolds number $= BV_0/\nu$
T, t mean and instantaneous temperature
ΔT mean temperature difference $= T_w - T_f$
T_c inverse function of I_c
T_m measurement period
T_f fluid temperature at the nozzle exit
T_{ref} reference temperature
T_w wall temperature
U, V, W X, Y, Z component of mean velocity
u, v, w X, Y, Z component of instantaneous velocity
v_m Y component of instantaneous measured velocity
v^* Y^* component of instantaneous velocity
V_0 nozzle exit velocity
X, Y, Z coordinate system based on flow geometry
X^*, Y^*, Z^* coordinate system based on camera geometry.

Greek symbols
α acceleration factor $= \partial V/\partial Y$
Γ circulation
δ_l laminar boundary layer thickness
Ω, ω X component of mean and instantaneous vorticity
φ camera angle
ν kinematic viscosity
σ standard deviation of ω'
τ time
ξ, η lag space for the spatial correlation or conditional average.

Superscript
$'$ fluctuating value.

(1). So the existence of Reynolds stress $\overline{v'v'}$ and the turbulent heat flux $\overline{v't'}$ (both are zero for laminar case) makes crucial difference of the heat transfer rate between laminar solution and actual turbulent flow. The coherent vortical structures observed in previous investigations mentioned before are expected to produce both of $\overline{v'v'}$ and $\overline{v't'}$. Thus the dynamic and spatio-temporal relationship between these quantity and the vortical structures are quite interesting to know about it, although it has not been done yet because of difficulties in measurement and evaluation of the coherent structures.

By our previous work [7, 8], a combined system for simultaneous measurements of velocity and temperature using digital particle image velocimetry (DPIV) and laser induced fluorescence (LIF) has been developed and applied to turbulent flows in order to clarify the role of coherent structures in the heat transfer. This technique provides us with spatio-temporal distributions of quantities related to convective heat transfer. The DPIV, which has the advantage of being able to process a greater number of velocity vectors than other technique like particle tracking velocimetry (PTV), permits a measurement of the vorticity component normal to the measuring plane. In the present study we applied these techniques to the stagnation region of a plane impinging water jet in order to clarify the detailed mechanism of heat transfer by investigating the spatio-temporal distribution of vorticity and turbulent heat flux.

2. EXPERIMENTAL METHOD AND PROCEDURE

2.1. *Flow apparatus*

The flow system employed in the present investigation is shown schematically in Fig. 1. A water jet issuing upward from a rectangular nozzle impinges on a horizontal, electrically-heated surface. Note that in order to supply the jet, the entrainment flow from the surrounding fluid also flowed in the same direction as the jet with a uniform velocity at 5% of the jet velocity. The nozzle exit was $B = 14.5$ mm in width and 150 mm in span. The jet had a uniform velocity profile at the nozzle exit and the streamwise turbulence intensity was about 1.5%. The hot surface was 130×145 mm and was made of a 3 mm thick Bakelite base plate covered with five strips of 130×29 mm in area and 30 μm thick stainless steel foil heater. All the strips were not glued onto the base plate, just in tension to allow the lengthwise thermal expansion of the foil and electrically connected in series to supply the d.c. current. A copper-constantan thermocouple of 100 μm in diameter was attached on the backside of the foil at the center of the plate ($X = Z = 0$ mm). In order to reduce the formation of the bubble on the heated

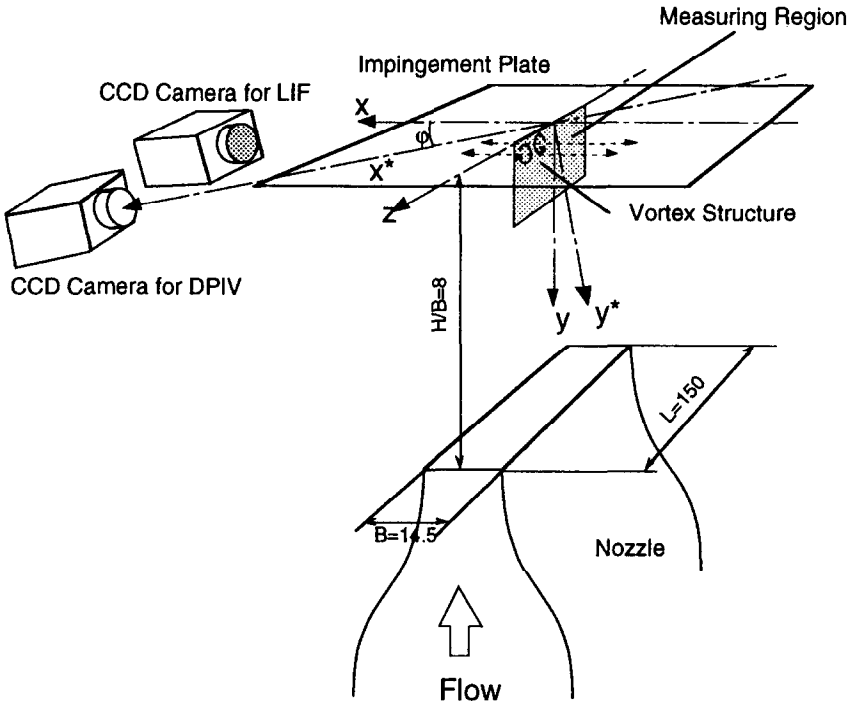

Fig. 1. Experimental apparatus and coordinate system.

surface, the working fluid was heated up to 95°C to get out the air in the water.

As the spacing between longitudinal vortices on the surface is independent with Reynolds number ranging from 2000 to 20 000 [5], the jet Reynolds number was held constant at 2000 based on the nozzle exit velocity $V_0 = 107$ mm/s and the nozzle width B. A dimensionless nozzle-to-plate spacing H/B was set at 8 which Gardon *et al.* [1] reported as giving the maximum heat transfer rate at the stagnation point. The averaged heat flux from wetted surface of the foil was $q_w = 44$ kW/m^2. This value was calculated by evaluating the heat generated from the foil with compensation due to heat loss through the backside of the Bakelite base plate. The average temperature difference between the hot surface and the fluid was 14.3 K.

The coordinate system used for data presentation is defined in Fig. 1. The origin is located at the center of the plate. The X-axis is normal to the jet flow and normal to the stagnation line, the Y-axis is normal to the plate and Z-axis is the stagnation line itself.

2.2. *Measurement techniques of velocity and temperature*

Digital particle image velocimetry (DPIV) was employed to obtain the velocity vectors at each location in the video images of the flow field. The velocity vectors are calculated from the displacement within a small domain of single exposure double-frame images and the time interval between each exposure. The displacement is obtained from the location of the maximum cross-correlation function between the small domains. In order to compute the displacement with sub-pixel accuracy, the location was evaluated from a Gaussian function fitted to the cross-correlation function. We used conventional NTSC video equipment with a framing rate of 30 frames a second. Illumination of tracer particles by single laser pulse per frame would thus provide a time interval of 1/30th of a second. This interval is too long for the high shear rates we are studying and for many applications. To get around this problem the flow field was illuminated at the end of the first exposure period of the CCD as a first pulse and at the start of the second exposure period as a second pulse. Therefore the time interval between pulses, which is independent of the camera's framing rate, could be varied from sub-micro second to 1/30th of a second.

Laser induced fluorescence (LIF) was applied for temperature measurement by utilizing the dependence of the intensity of fluorescence on the temperature [7]. When the concentration of fluorescence dye and the intensity of the incidence light are constant, the temperature is expressed as:

$$T(x,y) = T_c\left(I_c(T_{ref})\frac{I(x,y)-I_b(x,y)}{I_{ref}(x,y)-I_b(x,y)}\right) \quad (3)$$

where I_c is the calibration function of the fluorescence intensity to temperature, T_c is the inverse function of I_c, I_{ref} is the fluorescence intensity at a reference fluid temperature T_{ref}, I_b is the fluorescence intensity when there is no incidence light. T_c and I_c were experimentally obtained. As the fluorescence dye, Rhodamine B, used in the present experiments has a peak emission wavelength at $\lambda_e = 600$ nm, a peak absorp-

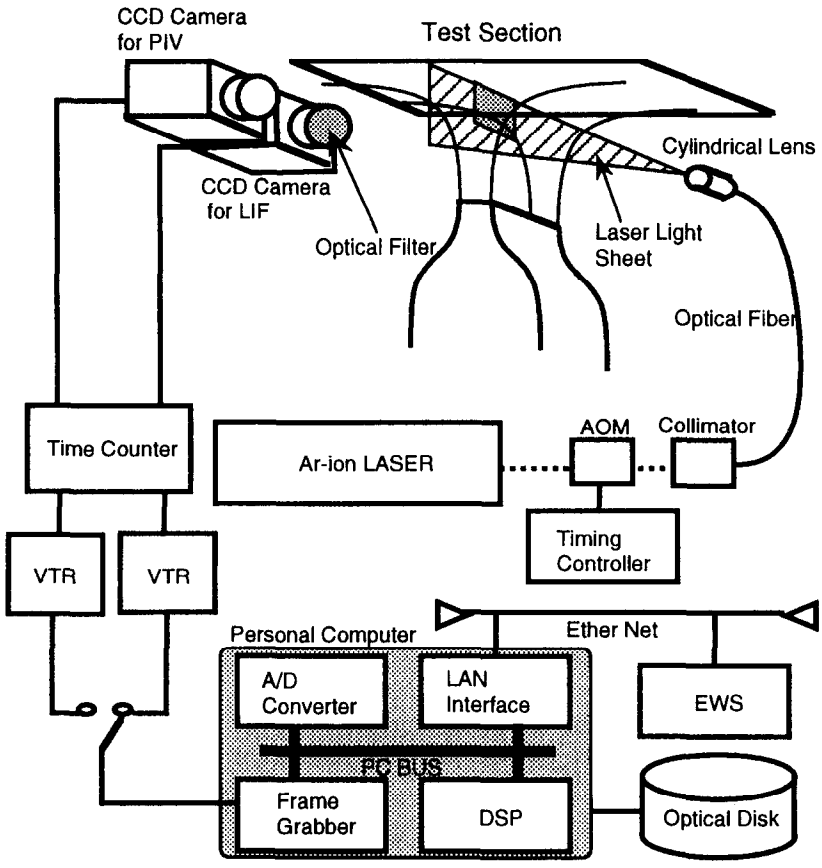

Fig. 2. Measurement system.

tion wavelength at $\lambda_a = 540$ nm and the wavelength of the incident light (Are-ion laser) is $\lambda_i = 514.5$ nm, we placed an optical filter that cut the wavelength λ_i on the CCD camera so that the scattering light of the tracer particles would be eliminated.

Figure 2 illustrates the measuring system. The water flow was marked with the tracer particles (15 μm polyethylene, Sumitomo-seika HE-5023) for velocity and with the fluorescence dye, Rhodamine B, for temperature. A measurement plane was illuminated by a laser light sheet using a 4W Ar-ion laser. The pulse width and the interval of the laser sheet were controlled synchronously with two CCD cameras (768×494 pixel, SONY XC-75) which viewed the same measurement region. Synchronized stroboscopic illuminations were generated by an acousto–optical modulator cell (Model A-160, HOYA) chopping the laser beam. Video signals from the CCD cameras were recorded on separate VCRs (NTSC S-VHS, AG-5700 Panasonic). A bar-code field number was superimposed onto each video field to tag the image frames. The temperature distribution and the velocity vectors were computed from recorded images by using PC's CPU and Texas Instruments, TMS320C31 digital signal processor (DSP) which accelerates the calculation of the cross-correlation function. It was felt by experience that, with a smaller computer system, the processing procedures should be accelerated to obtain the velocity and temperature as soon as possible while conducting the experiments.

2.3. *Measuring region and uncertainty*

The counter rotating vortex pairs in the stagnation region of the plane impinging jet has a major axis parallel to the X-axis and extends across the stagnation line, Z-axis [5]. Therefore, it is expected that the vorticity components, ω_x, is dominant in comparison to the other component. To evaluate ω_x and to clarify the relation between heat transfer and vorticity, the velocity components v and w in Y–Z plane on Z-axis were measured. The measurement region had an area of 20×20 mm^2 located near the origin since the distance between the vortex pairs is comparable to the nozzle width B as shown by Yokobori *et al.* [5]. A calibration plate etched with a regular grid on its surface was put in the measurement region and permitted a correspondence between the actual position and pixel position in the images to be established.

A density gradient induced by a temperature gradient in the thermal boundary layer refracts the scattering light from the tracer particles and fluorescence light of the dye. This causes a distortion and smearing of the images. The light parallel to the wall is refracted the most, since the path of the incident light in the boundary layer is the longest. To reduce the light path in the boundary layer and to avoid the distortion of

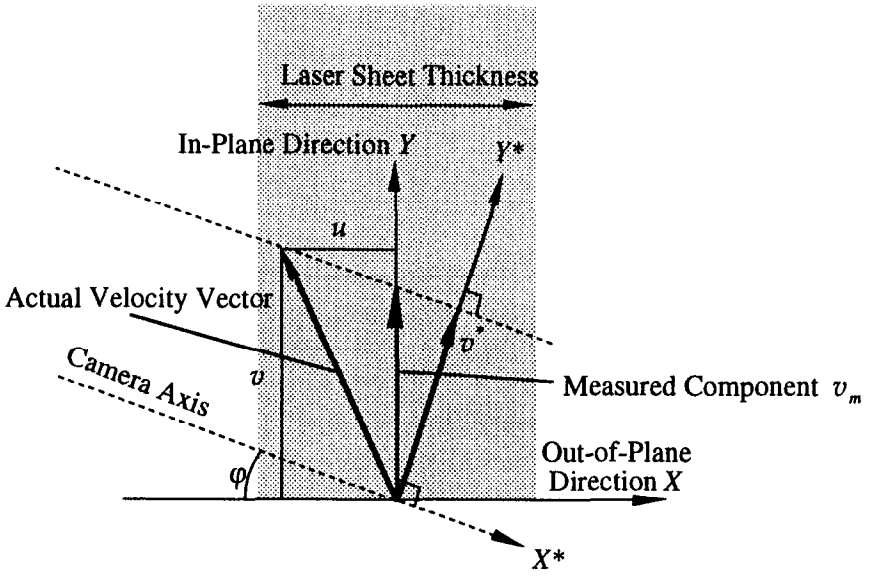

Fig. 3. Geometrical configuration of the camera axis and measured velocity vector.

the images, the major axis of the CCD camera was tilted at the angle of $\varphi = 22^\circ$ as shown in Fig. 1. However, the measured component of the velocity is different for this angle from a case without tilting. The geometrical configuration of measured and targeted vector are given in Fig. 3, where X^* is the camera axis. Obviously in this figure the Y-component of the measured velocity vector is v_m. Thus, v is obtained by:

$$v = v_m - u\tan\varphi. \tag{4}$$

By assuming $U = 0$ along the stagnation line, the Y-component of the mean velocity is:

$$V = \bar{v} = \overline{v_m} - U\tan\varphi = \overline{v_m}. \tag{5}$$

The instantaneous v and second-order moment of v cannot be evaluated without knowledge of the instantaneous velocity, u, which is an out-of-plane component. Thus, instead of v, we defined the Y^*-component of velocity, v^*, as:

$$v_* = v_m\cos\varphi. \tag{6}$$

The results shown in the following sections use v^*.

An error analysis has been done for the present experiments. The uncertainty of the velocity measurement was ± 6.7 mm/s and the uncertainty of the temperature measurement was ± 1.2 K for 95% confidence. The major error factor originated from the evaluation process of the particle displacement for velocity measurement and from random noise of the CCD camera output for temperature measurement. The spatial resolution was $2\times1\times1$ mm^3 for velocity measurement and $2\times0.4\times0.4$ mm^3 for temperature measurement. The statistical analysis was based upon 3400 samples of velocity and temperature distribution with a time interval of 1/20th of a second.

3. RESULTS AND DISCUSSION

3.1. *Profile of mean and RMS quantity*

Figure 4 presents the mean and RMS velocity and temperature distributions averaged over Z-direction. By assuming Hiemenz flow [4] the mean velocity normal to the wall is given as

$$V = -\alpha Y \tag{7}$$

where the acceleration factor α had been experimentally obtained [9],

$$\alpha = V/B\cdot(1.02 - 0.024\,H/B). \tag{8}$$

Equation (7) in Fig. 4 is represented by a dashed line which is obtained by substituting $\alpha = 6.1(1/s)$ for the present experiments. As the experimental result on V is asymptotically fitted to equation (7), the reliability of the present experiment is confirmed.

The quantity $\sqrt{\overline{v_*'^2}}$ has a maximum near $Y/B = 0.2$ and rapidly decreases upon approaching the wall, while $\sqrt{\overline{w'^2}}$ is still increasing at $Y/B = 0.1$. The turbulence fluctuation normal to the wall is reduced by the wall effect, such as in the case for flow parallel to the wall. However, $\sqrt{\overline{v_*'^2}}$ is larger than $\sqrt{\overline{w'^2}}$ except near the wall region. This fact is perhaps the distinguishing feature of the impinging jet contrasted to flow parallel to the wall. The thickness of the thermal boundary layer is estimated to be $\delta_t/B \approx 0.1$ from the mean temperature profile.

3.2. *Instantaneous velocity and temperature field*

Figure 5 shows an instantaneous velocity and temperature map. In this figure the velocity vectors are superimposed on the temperature distribution represented in gray-scale. The spatial distribution of vectors, with a counterclockwise/clockwise vortex pair

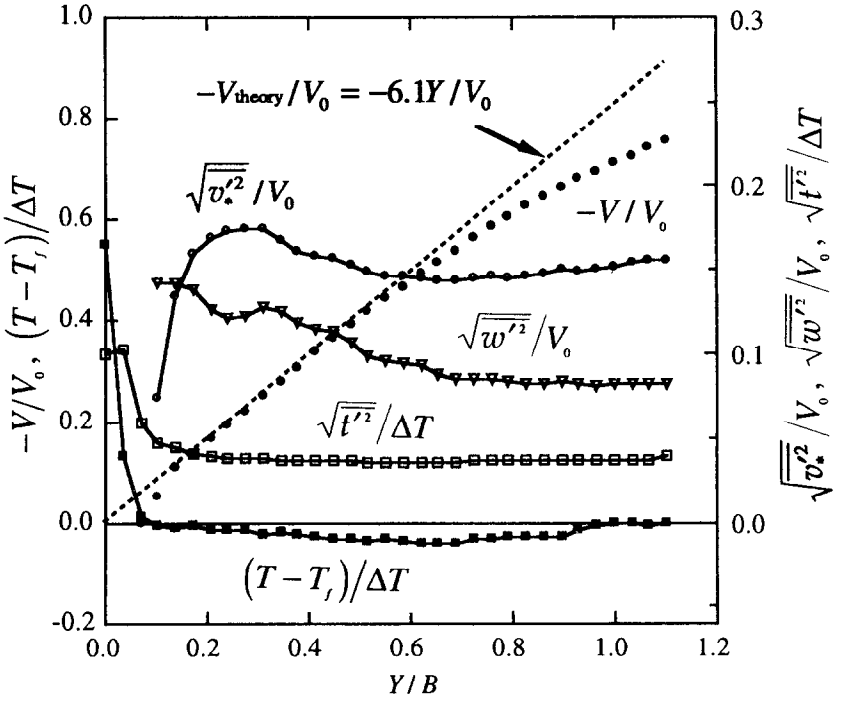

Fig. 4. Profile of mean and RMS quantity. Dashed line represent the theoretical value of the mean velocity component normal to the wall by assuming Hiemenz flow.

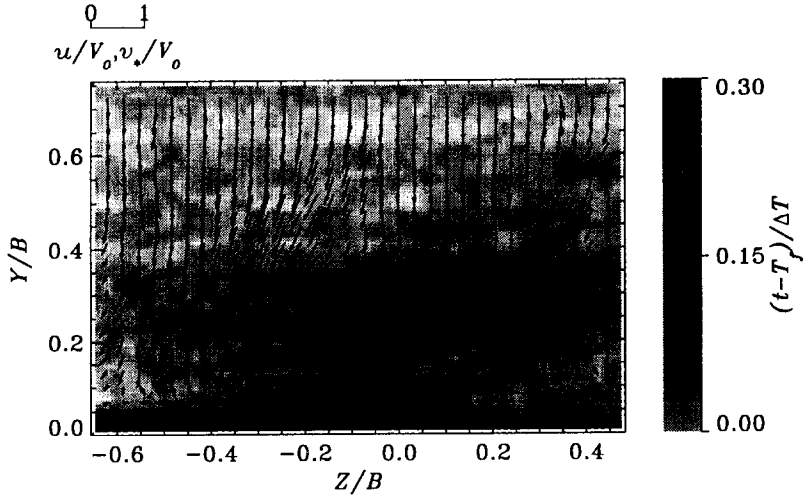

Fig. 5. Instantaneous velocity and temperature map.

and a vertical up flow between the vortices is typical. The fluid between the vortex pair is ejected toward the outer flow region by the vortices and the fluid on either side of the vortex pair is swept inward toward the wall. We refer to the former as the "upwash region" and the latter as the "downwash region". A high temperature layer at the wall is lifted upwards in the upwash region and heads to the outer flow region. In the downwash region, cold fluid directly impinges against the wall and depletes the boundary layer while sweeping hot fluid toward the center. Finally, the fluid moves away from the wall in the upwash region and discharge to the outer flow.

An instantaneous vorticity map corresponding to Fig. 5 is shown in Fig. 6. The vorticity was evaluated from circulation in order to reduce errors caused by differencing. The circulation is:

$$\Gamma = \oint_C v \cdot \mathrm{d}x = \iint_S \omega \cdot \mathrm{d}S \tag{9}$$

while the resulting vorticity is

$$\omega = \lim_{S \to 0} \frac{\Gamma}{S} = \lim_{S \to 0} \frac{1}{S} \oint_C v \cdot \mathrm{d}x. \tag{10}$$

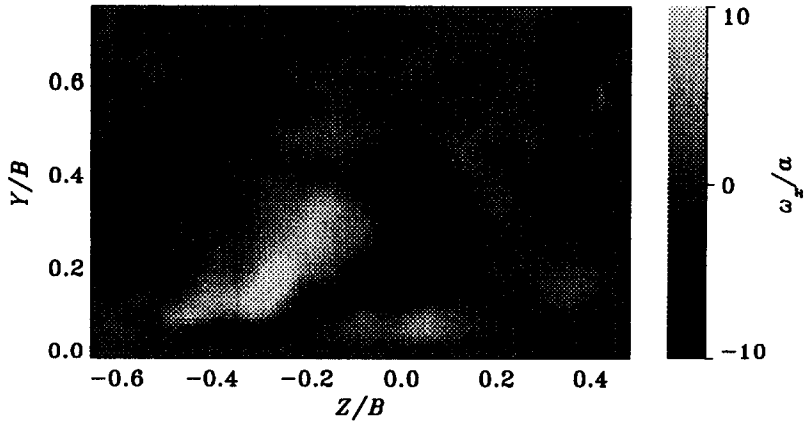

Fig. 6. Instantaneous vorticity map at same instant of Fig. 5.

As the velocity data are obtained on regular grids, the actual vorticity is evaluated from,

$$\omega \equiv (-u_{1,1}\Delta x - u_{0,1}\Delta x - v_{-1,1}\Delta y - v_{-1,0}\Delta y + u_{-1,-1}\Delta x + u_{0,-1}\Delta x + v_{1,-1}\Delta y + v_{1,0}\Delta y)/(4\Delta x\Delta y) \quad (11)$$

where the subscripts of velocity component u and v denote the grid distance from the grid point of ω, while Δx and Δy are the spacing between neighboring grids. In Fig. 6, negative (clockwise) and positive (counterclockwise) vorticity are, respectively, represented by black and white shades. The vorticity is normalized by the acceleration factor α and the maximum and minimum values of the vorticity are located in the center of the vortex. The uncertainty in the instantaneous vorticity was ± 9.4[1/s], estimated from the uncertainty in the velocity measurements.

The temperature distribution at $Y/B = 0.01$ in Fig. 5 is shown in Fig. 7. The fluid temperature in the upwash region, just under the vortex pair, is locally higher than that in the downwash region. Figure 8 indicates the temporal variation of the temperature measured by thermocouple just beneath the foil heater and LIF at $X/B = Z/B = 0$, $Y/B = 0.01$. The solid line also shows the tracking average of the LIF points. Although the temperature variation of the wall is delayed relative to the fluid, the trends agree with each other. This fact supports that the temperature

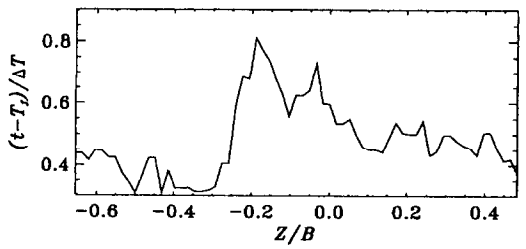

Fig. 7. Instantaneous fluid temperature profile in the vicinity of the wall. $Y/B = 0.01$ at same instant of Fig. 5.

distribution shown in Fig. 7 is qualitatively equal to the wall temperature distribution. By comparing the surface temperature on planar measured by Yokobori [5] and the surface temperature of blunt bodies by using liquid crystal sheet measured by VanFossen [6], the highest heat transfer rate was not under the vortices but at the location between neighboring vortex pairs where the vortex-induced velocity was directly toward the surface. These observations are consistent with the present results. Since a high temperature area expands upwards in the upwash region, an instantaneous thermal boundary layer becomes thicker, and the wall temperature just under the vortex pair increases in order to maintain the constant heat flux condition at the wall.

Figures 9 and 10 show representative temporal variations of the streamwise vorticity field. In Fig. 9 the instantaneous vorticity, whose absolute value is the maximum in the given Y location, is plotted against the time lapse τ. This Y–τ diagram enables us to see the movement of the vortices in the Y direction. The vortices are convected from an upstream location toward the wall (referred to by an arrow (1) in the figure) and intensifies the vorticity in the vicinity of the wall (approximately $Y/B = 0.3$) while "residing" near the wall with up and down motion (referred to by an arrow (2)). In Fig. 10, the instantaneous vorticity, whose absolute value is the maximum in the given Z location, is plotted against the time lapse τ in order to reveal the horizontal movement of the vortices in the Z-direction. The vortex pairs repeat movement in the Z-direction and disappear (as referred to by arrow (3)). Since the mean velocity gradient normal to the wall $\partial V/\partial Y$ increases upon approaching the wall (observed in Fig. 4), the streamwise velocity gradient $\partial U/\partial X$ should also increase due to continuity of the flow and the principal axis of the mean strain rate is directed along the X-axis. As the counter-rotating vortices are aligned with this axis, the vortices can stretch and intensify the vorticity since there is conservation of angular momentum. Continuous stretching of the vortices reduces the cross-sectional area

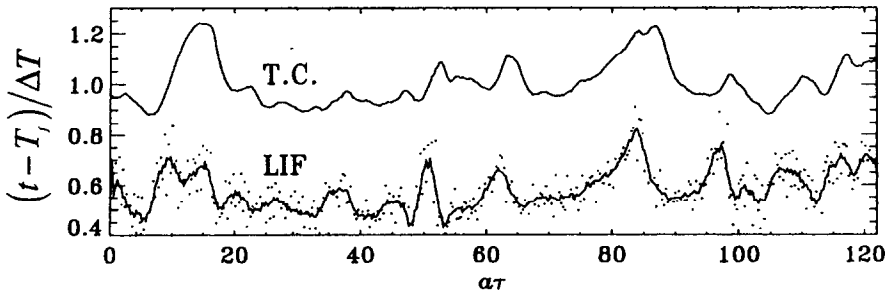

Fig. 8. Temporal variations of temperature measured by a thermocouple just beneath the foil heater and LIF at $X/B = Z/B = 0$, $Y/B = 0.01$.

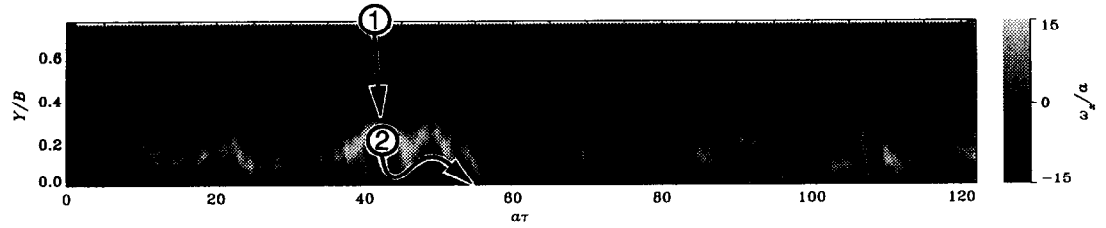

Fig. 9. Y-τ diagram of vorticity. Instantaneous vorticity whose absolute value is the maximum in the given Y location is plotted against the time lapse τ.

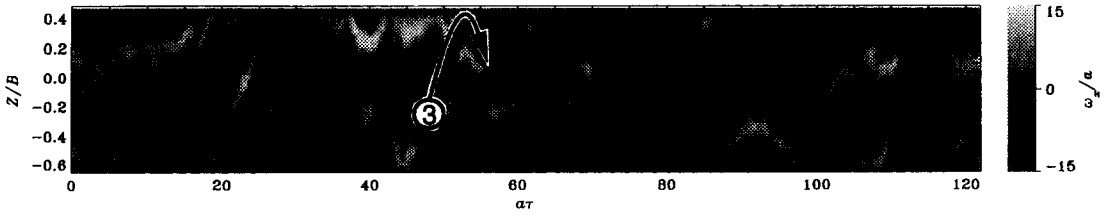

Fig. 10. Z-τ diagram of vorticity. Instantaneous vorticity whose absolute value is the maximum in the given Z location is plotted against the time lapse τ.

of the vortices and eventually these vortices are disappeared.

3.3. *Turbulent heat flux and weighted PDF*

A profile of turbulent heat flux is shown in Fig. 11. The turbulent heat flux reaches a maximum value $\rho C_p \overline{v'_* t'}/q_w = 0.18$ at $Y/B = 0.13$. This means that approximately 20% of the heat flux supplied by the wall is transported in a direction away from the wall by the turbulence fluctuations.

Figure 12 shows a weighted probability density function (WPDF) of the turbulent heat flux, which is defined as,

$$W(v'_*, t') = \rho C_p v'_* t' P(v'_*, t')/q_w \qquad (12)$$

where $P(v', t')$ is the joint probability density function of $\rho C_p \overline{v'_* t'}/q_w$. The integrated value of this function in each quadrant indicates the fractional contribution of the quadrant to $\rho C_p \overline{v'_* t'}/q_w$ and integration over the whole v'-t' plane equals the conventional time-averaged $\rho C_p \overline{v'_* t'}/q_w$. Note that the first quadrant ($v' > 0$ and $t' > 0$) has a larger contour spread for v' and t' and subsequently larger integrated value than the third quadrant ($v' < 0$ and $t' < 0$). This means that the ejection of the hot fluid from the wall contributes more to the positive turbulent heat flux than the down-sweep of cold fluid to the wall region. Since the contour extends further in the positive direction of v', larger velocity fluctuations describing ejection from the wall are dominant.

3.4. *Turbulent heat flux and counter rotating vortex pairs*

The generation of the turbulent heat flux is strongly related to the structure of the counter-rotating vortex pairs with the upwash between vortices. Figure 13 shows a temporal variation of instantaneous turbulent heat flux distributions at $Y/B = 0.13$. The elongated shapes corresponding to higher turbulent heat flux at $\alpha\tau = 20$, 65, 100 (as referred to by arrows) are observed in this figure and the location of these regions matches that of the counter-rotating vortex pairs shown in Fig. 10. Especially, higher turbulent heat flux is generated in the middle of the counter-rotating vortex pair when the upwash of the fluid transports the heat from the wall.

The relation between counter-rotating vortex pairs and the turbulent heat flux is statistically quantified by the following spatial-correlation function:

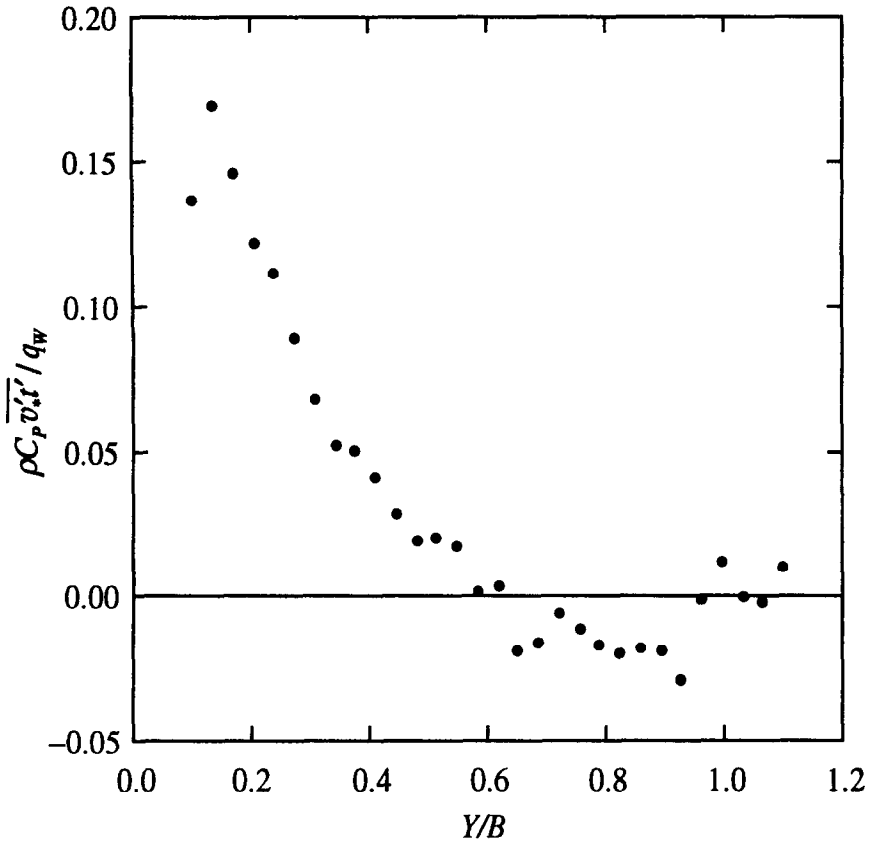

Fig. 11. Profile of turbulent heat flux.

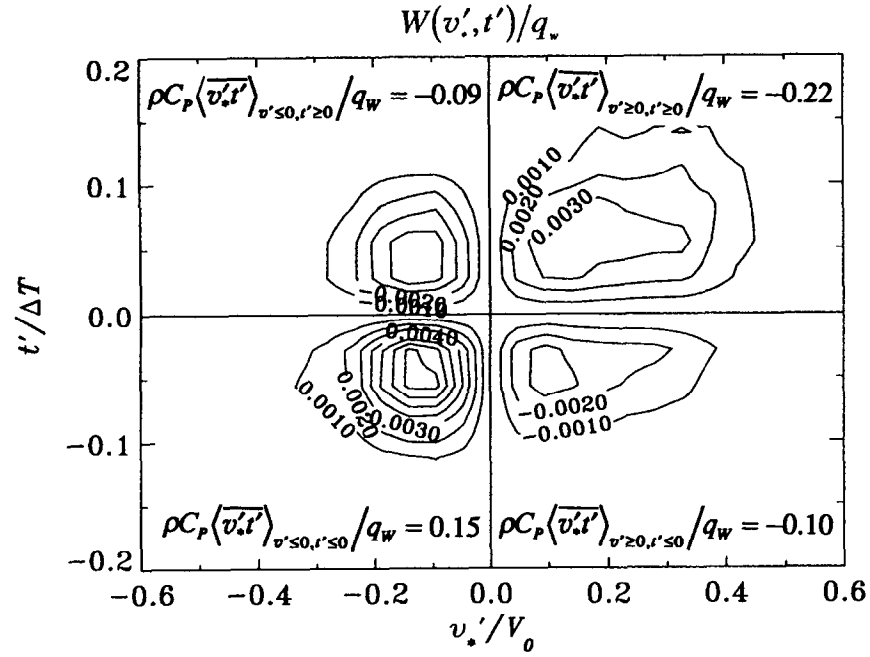

Fig. 12. Contour of the weighted probability density function of turbulent heat flux.

$$R_{v_*\omega}(y, z, \eta, \xi) = \frac{\overline{v'(y,z)t'(y,z)\omega_x'(y+\eta, z+\xi)}}{\sqrt{\overline{\{v'(y,z)t'(y,z)\}^2}}\sqrt{\overline{\omega_x'^2(y+\eta, z+\xi)}}}. \quad (13)$$

The value of $R_{v_*\omega}$ is plotted in Fig. 14 for the fixed point $(y/B, z/B) = (0.14, -0.24)$ and for $\eta = 0$ as a function of ξ. The minimum and maximum values are located at $\xi/B = 0.1$ and -0.1, respectively. This

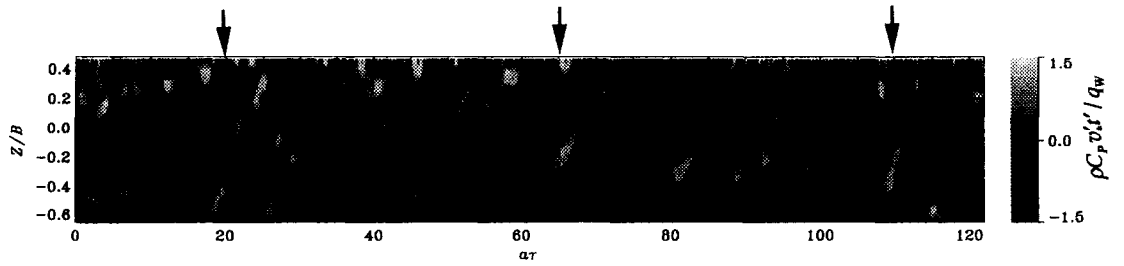

Fig. 13. Z-τ diagram of the instantaneous turbulent heat flux at $Y/B = 0.13$.

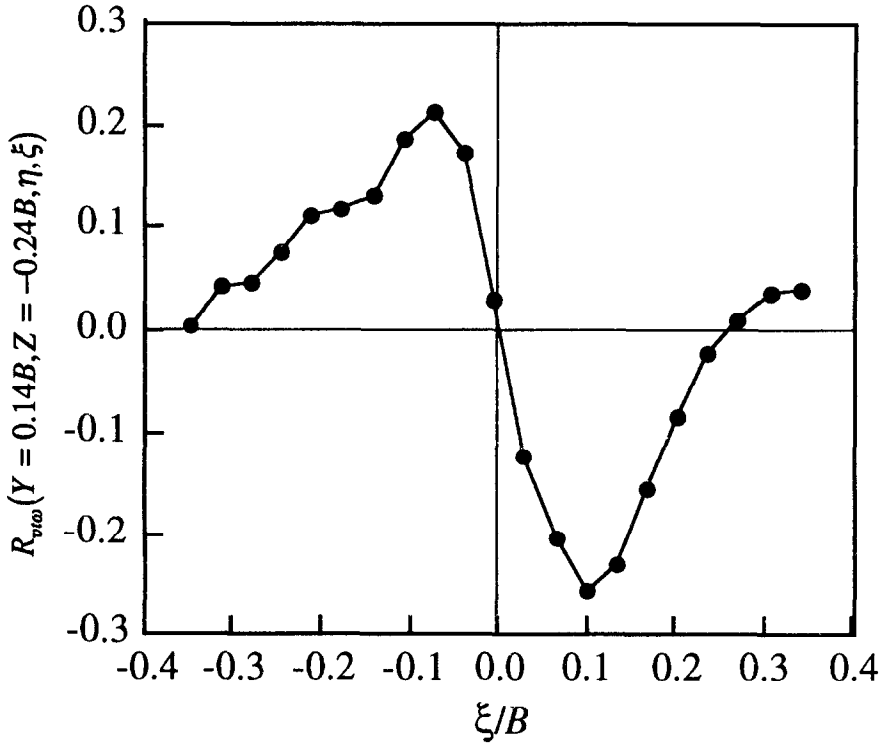

Fig. 14. Spatial correlation of turbulent heat flux and vorticity.

means that the location where high turbulent heat flux is generated has a higher probability of existence of a counterclockwise vortex at the left (direction of negative ξ) and the clockwise vortex at the right (direction of positive ξ). Consequently the high turbulent heat flux is generated in the upwash region between counter-rotating vortices.

The counter-rotating vortices, however, do not continue to stay at the same location. As mentioned before, those vortices are convected away in spanwise direction or just disappear by dissipating into heat. Therefore, an evaluation of the fraction of the turbulent heat flux generated when the counter-rotating vortices "exist" on the wall surface is necessary to discuss the role of those vortices. Here we define a condition flag c as

$$\left.\begin{aligned} \text{if } \omega(Y,Z,\tau) \geqslant \omega_{\text{th}} \quad & c(Y,Z,\tau) = 1 \\ \text{otherwise} \quad & c(Y,Z,\tau) = 0 \end{aligned}\right\} \tag{14}$$

where ω_{the} is a positive threshold value which provides the existence of counterclockwise vortex. Then the conditional averaged turbulent heat flux is defined:

$$\langle v't' \rangle = \frac{1}{T_{\text{m}}} \int_0^{T_{\text{m}}} v'(Y, Z+\xi, \tau) \cdot t'(Y, Z+\xi, \tau) \cdot c(Y, Z, \tau)\, d\tau. \tag{15}$$

Figure 15 shows distributions of $\langle v't' \rangle$ normalized by a time averaged turbulent heat flux. Here the Y in equations (14) and (15) was chosen as $0.2B$, then function $\langle v't' \rangle$ for each Z was averaged over the spanwise length of the measuring region. For any ω_{th}, there is a peak at $\xi/B = 0.1$ which is explained as the right side (direction of positive ξ) of the counterclockwise vortex generating a significant turbulent heat flux. This is expected because the counter-rotating vortex pairs are formed by counterclockwise vortex at the left side and clockwise vortex at the right side and the middle of these vortices (is right side of the counterclockwise vortex) ejects hot fluid away from the wall.

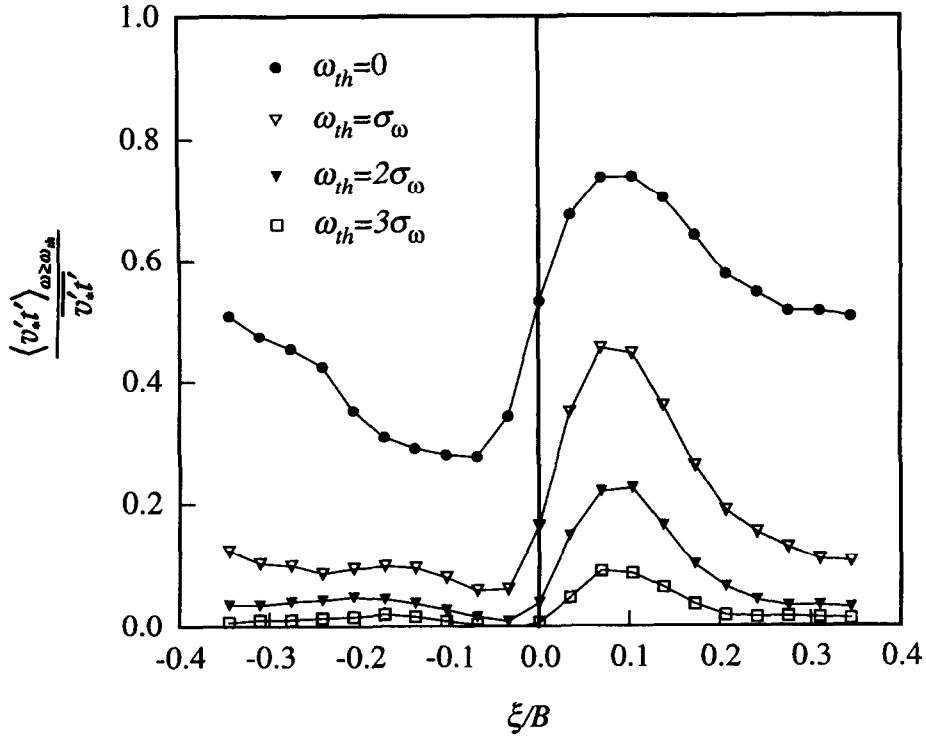

Fig. 15. Conditional averaged turbulent heat flux $\langle v't' \rangle$.

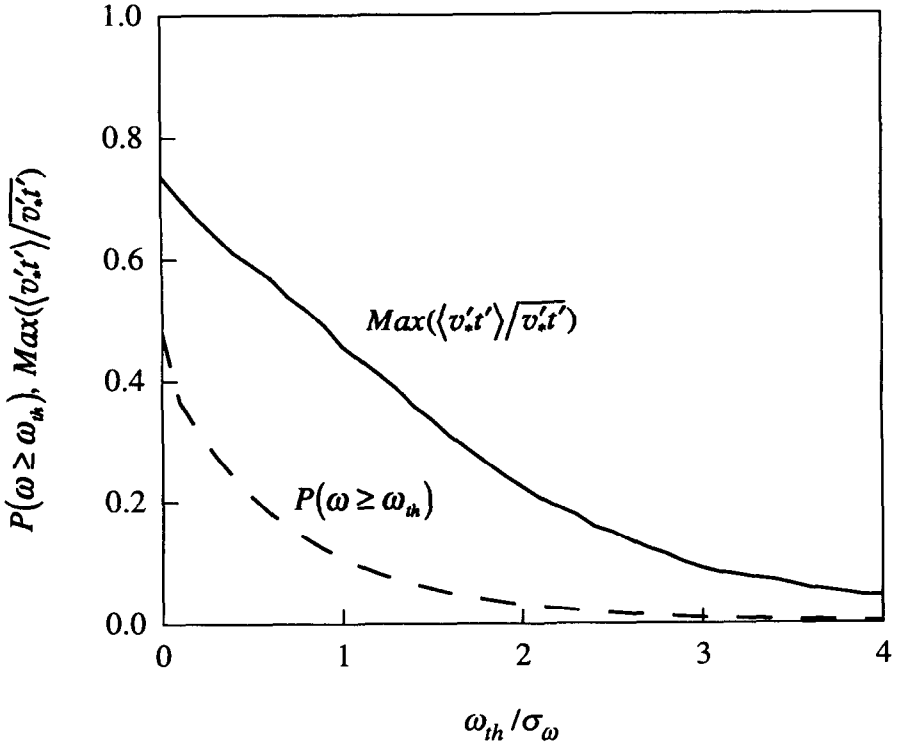

Fig. 16. Variation of the peak value of $\langle v't' \rangle$ and probability of $\omega > \omega_{th}$.

A variation of the peak value of $\langle v't' \rangle$ is shown in the Fig. 16 with a probability of $\omega > \omega_{th}$ as a function of ω_{th}. At the case of $\omega_{th} = 1\sigma_\omega$, although the time fraction of the existence of the vortex is less than 10%, approximately 45% of the turbulent heat flux is generated by this vortex. Furthermore, at the case of $\omega_{th} = 2\sigma_\omega$ and $3\sigma_\omega$, the vortex exists only 3 and 1% in time, 20 and 10% of turbulent heat flux is generated,

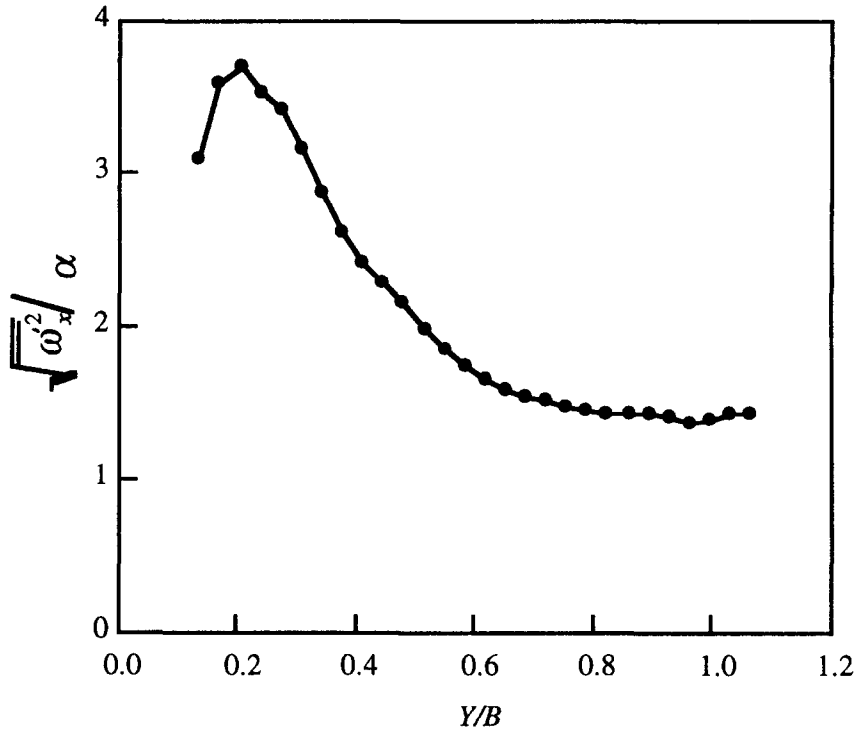

Fig. 17. Profile of the standard deviation of the fluctuating vorticity.

respectively. Although the counter-rotating vortices do not always exist at the same location, the turbulent heat flux can be produced by those vortices in fairly small fraction of the time.

From these arguments it is apparent that the counter-rotating vortex pairs significantly contribute to the generation of turbulent heat flux in the vicinity of the wall through the upwash of the fluid from the wall.

3.5. *Transport mechanism of the counter-rotating vortex pair*

As stated, before a counter-rotating vortex pair in the stagnation region of the jet is a typical coherent structure in the vicinity of the wall and the upwash by this vortex pair plays an important role in the transport of heat from the wall. The present section describes the mechanism of this generation and transport of vorticity.

Figure 17 shows the profile of the standard deviation of the fluctuating vorticity $\sqrt{\overline{\omega_x'^2}}/\alpha$. The values increase upon approaching the wall and reach maximum at $Y/B = 0.2$. In other words, the vortices are convected downstream and they increased in vorticity content in the vicinity of the wall as shown in Fig. 9. Sutera *et al.* [2, 3] simulated the counter-rotating vortex, pairs in the Hiemenz flow. They found that the vorticity, for a spatial scale 2.6 times larger than the Hiemenz boundary layer thickness was amplified by the flow diverging in the X-direction. Lyell and Huerre [10] analyzed the linear and nonlinear stability problems originating from the concave streamline curvature in the stagnation region. They concluded that the centrifugal force was insignificant compared to the viscosity so that the disturbances added to the flow are attenuated and stabilized. Therefore, it appears likely that the counter-rotating vortex pairs originate from the free jet region and not from the instability of the concave streamline curvature in the stagnation region, and are convected downstream where they are selectively intensified by vortex-stretching in the X-direction. As suggested by Yokobori [5] the counter-rotating vortices was not observed if the nozzle-to-plate spacing was shorter than the length of the potential core. It is supposed that the interaction between spanwise rollers in both shear layer of the jet causes X-component of vorticity in the center plane of the jet and leads to the counter-rotating vortices.

The mechanism of the vorticity transport is revealed by examining the transport equation of the mean-square vorticity fluctuation [11]. Assuming the two-dimensionality of the mean flow, $W = \Omega_x = \Omega_y = 0$, assuming the symmetry of the flow on the stagnation line, $U = \Omega_z = S_{12} = S_{13} = 0$ and neglecting terms of the first- and second-order derivatives in the Z-direction, the transport equation of the mean-square vorticity fluctuation becomes:

$$V\frac{\partial}{\partial Y}\left(\frac{1}{2}\overline{\omega_x'\omega_x'}\right) \quad (A)$$

$$-\overline{\omega_x'\omega_x'S_{xy}}-\overline{\omega_x'\omega_y'S_{xy}}-\overline{\omega_x'\omega_z'S_{xz}} \quad (P_t)$$

$$-\overline{\omega_x'\omega_x'}S_{xy} \quad (P_m)$$

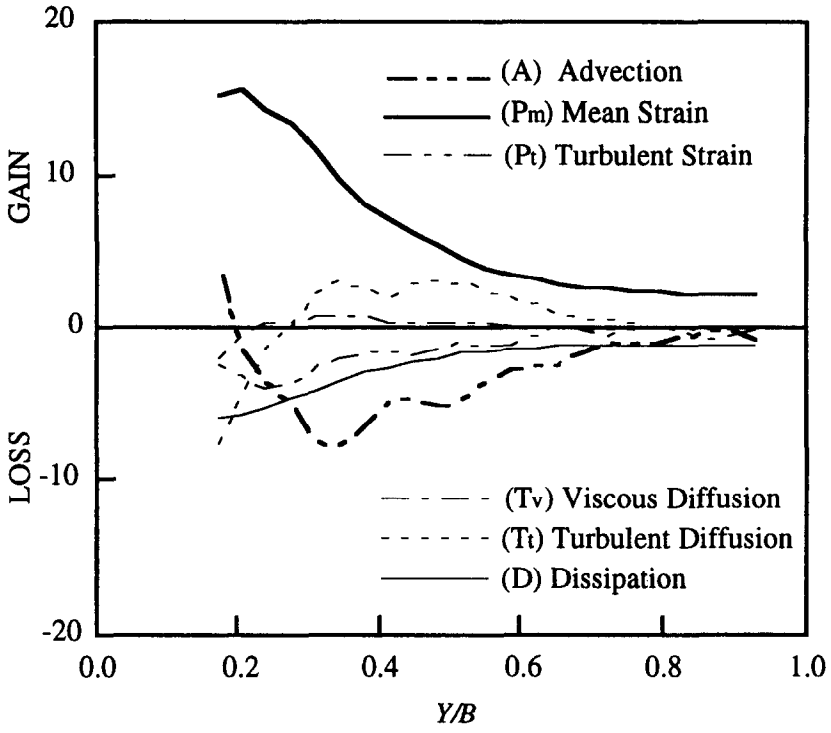

Fig. 18. Budget of the equation for the mean-square vorticity fluctuation.

$$+\frac{1}{2}\frac{\partial}{\partial X}(\overline{u\omega_x'\omega_x'})+\frac{1}{2}\frac{\partial}{\partial Y}(\overline{v\omega_x'\omega_x'}) \quad (T_t)$$

$$-\nu\frac{\partial^2}{\partial X^2}\left(\frac{1}{2}\overline{\omega_x'\omega_x'}\right)+\nu\frac{\partial^2}{\partial Y^2}\left(\frac{1}{2}\overline{\omega_x'\omega_x'}\right) \quad (T_v)$$

$$+\nu\overline{\frac{\partial\omega_x'}{\partial X}\frac{\omega_x'}{\partial X}}+\nu\overline{\frac{\partial\omega_x'}{\partial Y}\frac{\partial\omega_x'}{\partial Y}}+\nu\overline{\frac{\partial\omega_x'}{\partial Z}\frac{\partial\omega_x'}{\partial Z}} \quad (D)$$

$$=0 \quad (16)$$

where the rate of strain is

$$S_{ij}=\left(\frac{\partial U_i}{\partial X_j}+\frac{\partial U_j}{\partial X_i}\right)s_{ij}=\left(\frac{\partial u_i}{\partial X_j}+\frac{\partial u_j}{\partial X_i}\right). \quad (17)$$

In equation (16), (A) is the advection, (P_t) is the production of the mean-square turbulent vorticity by turbulent stretching of turbulent vorticity, (P_m) is the production of turbulent vorticity caused by the stretching of vorticity fluctuations at the mean rate of strain S_{ij}, (T_t) is the transport of mean-square turbulent vorticity by turbulent velocity fluctuations, (T_v) is viscous transport and (D) is viscous dissipation. The first term of (T_t) and (T_v) were neglected by assuming the line-symmetry of the flow, the first term of (D) was neglected by assuming that the vorticity gradient in the X-direction is smaller than in other directions. From the continuity of the mean flow the mean rate of strain has the relationship $S_{xx}=S_{yy}$ that results in $(P_m)=\overline{\omega_x'\omega_x'}S_{yy}$. The other terms were calculated from experimental data and (P_t) is as the remainder of the equation. Thus a budget of each term when normalized by α^3 appears as shown in Fig. 18. The mean-square turbulent vorticity is mainly produced by the term (P_m) and balance with the convection and the viscous dissipation. This fact shows us that the amplification of the vorticity in the vicinity of the wall is caused by stretching of the counter rotating vortex pairs for X-direction by the strain in the mean flow. This amplification of the vorticity has a main role of the augmentation of the heat transfer in the stagnation region of the impinging jet.

4. CONCLUSION

We have presented a study on heat transfer and vortex structure in the stagnation region of a plane impinging jet. Instantaneous and time dependent velocity and temperature distributions in a plane parallel to the stagnation line in the vicinity of the wall were measured by a combined technique of digital particle image velocimetry (DPIV) and laser induced fluorescence (LIF).

Counter rotating vortex pair with upwash between the vortices and downwash at both side of the vortex pair were observed in the stagnation region. Instantaneous velocity and temperature maps showed that the counter rotating vortex pairs were convected from an upstream location, stayed near the wall surface experienced an elongation in the X-direction by the diverging flow of the impinging jet and as a result exhibited an amplified vorticity. The wall temperature in the upwash region, just under the vortex pair, was locally higher than downwash region where the cold fluid directly impinged onto the wall. A weighted

probability density function of the turbulent heat flux showed that the ejection of the hot fluid from the wall by the upwash mainly contributes to the net turbulent heat flux. A spatial correlation between the vorticity and the turbulent heat flux, the conditional averaged turbulent heat flux for various threshold value of the vorticity provided that the counter rotating vortex pair was attributed to the most probable structure to generate the turbulent heat flux. Terms in the equation of the mean-square vorticity fluctuations were evaluated directly from the experimental data and the stretching of the vortices by the diverging flow amplified the vorticity. This amplification of the vorticity enhanced the heat transfer in the stagnation region of the plane impinging jet.

Acknowledgements—Authors acknowledge a student Mr D. Hayashi of Keio University who participated in these experiments. Authors are thankful to Dr A. Tokuhiro of Power Reactor & Nuclear Development Corporation in Japan for his helpful discussions. This work was partly supported by a grant in aid for scientific research by the Ministry of Education of Japan under Grant no. 04555050.

REFERENCES

1. Gardon, R. and Akfirat, J. C., The role of turbulence in determining the heat transfer characteristics of impinging jet. *International Journal of Heat and Mass Transfer*, 1965, **8,** 1261–1272.
2. Sutera, S. P., Maeder, P. F. and Kestin, J., On the sensitivity of heat transfer in the stagnation-point boundary layer to free-steam vorticity. *Journal of Fluid Mechanics*, 1963, **16,** 497–520.
3. Sutera S. P., Vorticity amplification in stagnation-point flow and its effect on heat transfer. *Journal of Fluid Mechanics*, 1965, **21**(3), 513–534.
4. Schlichting, H., *Boundary-Layer Theory*. McGraw-Hill, New York, 1979.
5. Yokobori, S., Kasagi, N. and Hirata, M., Transport phenomena at the stagnation region of a two-dimensional impinging jet. *Transactions of JSME B* 1983, **49**(441), 1029–1039 (in Japanese).
6. VanFossen Jr, G. J. and Simoneau, R. J., A study of the relationship between free-stream turbulence and stagnation region heat transfer. *Transactions of ASME*, 1987, **109,** 10–15.
7. Sakakibara, J., Hishida, K. and Maeda, M., Measurements of thermally stratified pipe flow using image-processing techniques. *Experiments in Fluids*, 1993, **16,** 82–96.
8. Sakakibara, J., Hishida, K. and Maeda, M., Quantitative visualization of convective heat transfer near the stagnation region of an impinging jet. *ASME FED*, 1993, **172,** 93–99.
9. Martin, H., *Advances in Heat Transfer*, Vol. 13. Academic Press, New York 1977.
10. Lyell, M. J. and Huerre, P., Linear and nonlinear stability of plane stagnation flow. *Journal of Fluid Mechanics*, 1985, **161,** 295–312.
11. Tennekes, H. and Lumley, J. L., *A First Course in Turbulence*. MIT Press, MA, 1972.